# Modification and Characterisation of Zeolite Beta as a Possible Basic Catalyst for Biodiesel Production

BORDONHOS, Marta[a,b,*]; HENRIQUES, Carlos[a]; ZHOLOBENKO, Vladimir[b]

[a]*Instituto Superior Técnico, Universidade de Lisboa, Avenida Rovisco Pais, 1049-001 Lisboa, Portugal*
[b]*Keele University, Keele, Staffordshire, ST5 5BG, United Kingdom*

## ABSTRACT

The ever growing worldwide consumption of energy, associated with non-renewable fossil fuels, has led to an increasing interest in the field of renewable energy sources such as biodiesel.

Biodiesel is most commonly produced by the transesterification of animal fats or vegetable oils. Basic zeolites appear to be a good choice as heterogeneous catalysts for this process, due to their highly porous structure and reusability.

The acid form of zeolite beta (BEA-150, $SiO_2/Al_2O_3$ = 300) was subject to modification techniques in order to increase its basicity, by substituting its native $H^+$ with $K^+$. Seven samples were prepared: three by wet impregnation ($KNO_3$, K/Al = 1; KOH, K/Al = 2, 10) and four by ion exchange ($KNO_3$, K/Al = 1, 10; KOH, K/Al = 2, 10). The eight (original and modified) samples were calcined at 500 ºC for 4 hours.

The following characterisation techniques have been used: SEM/EDS, XRD, FTIR and $N_2$ sorption experiments. In FTIR, pyridine was used to probe the acidity of the eight uncalcined samples, and acetylene for the basicity of the eight calcined samples. In $N_2$ sorption experiments, MultiPoint BET and *t*-plot method were used to determine total and external and micropore surface areas; pore size distribution and diameter were determined by DFT.

Results have shown that samples treated with a 10-fold molar excess of KOH have suffered severe structural damage caused by desilication and dealumination.

SEM/EDS has shown a particle size of approximately 1 µm, although this may correspond to agglomerates of smaller particles. XRD patterns have shown that the samples are composed of around 50 – 60% of polymorph B. FTIR has detected a small amount of strong BAS and LAS. Increased basic character has been detected by redshifts in acetylene post-adsorption spectra. Excluding destroyed samples, the average values (for the remaining 12 samples) of MultiPoint BET surface area, *t*-plot method micropore volume and DFT pore diameter were, respectively, 512 $m^2/g$, 0.113 $cm^3/g$ and 9.2 Å.

**Keywords:** zeolite, BEA-150, characterisation, modification, catalyst, biodiesel

## 1. INTRODUCTION

In a world reliant on non-renewable fossil fuels as a means to obtain energy, biodiesel production is becoming an ever more viable, reliable and ecological alternative [1].

Biodiesel is the designation given to the renewable fuel that originates from the conversion of lipid feedstocks rich in triacylglycerols (TAG), such as animal fats or vegetable oils, into fatty acid alkyl esters (FAAE). The production of biodiesel can be achieved through a number of different processes although the most commonly used is the catalysed alcoholysis of the lipid feedstocks into FAAE and glycerol, known as transesterification. In this reaction, one molecule of TAG reacts with three molecules of the chosen alcohol, typically methanol or ethanol, to generate one molecule of glycerol and three molecules of FAAE, as shown step-by-step in Figure 1.

Amidst the catalysts available to be used in the alcoholysis process, two major groups can be identified: homogeneous and heterogeneous. Inside these two groups the catalysts can be classified as acidic, basic or a combination of the previous two, i.e., bi-functional [1] [2]. For biodiesel production, heterogeneous catalysts are usually preferred due to certain characteristics as ease of catalyst-product separation and possibility of catalyst regeneration and reuse, with the basic types being favoured over the acid types,

* Corresponding author.
*E-mail address*: marta.bordonhos@tecnico.ulisboa.pt

due to the former's more advantageous characteristics, such as faster reaction rates, mild reaction conditions, low cost and wide availability [2].

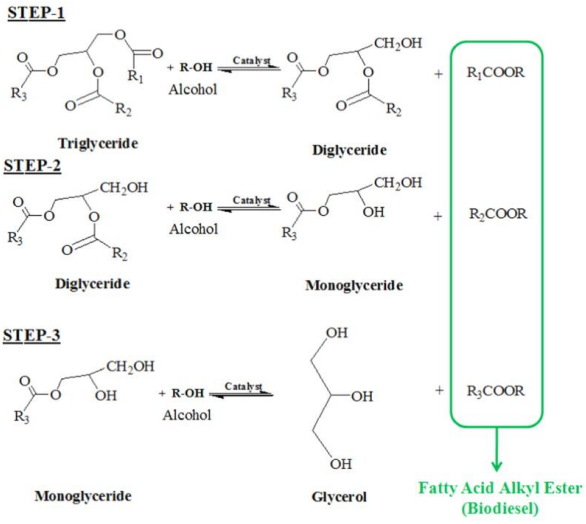


**Figure 1 –** Transesterification of TAG into FAAE (biodiesel) [1]

Of the many available catalysts, zeolites are the most versatile, due to their modifiable chemical composition and pore size distribution [3]. The acid-base properties and shape selectivity of these molecular sieves can be adjusted via modification techniques, such as wet impregnation, ion exchange or calcination. In addition to being used as catalysts, zeolites are also widely used as adsorbents and in the composition of detergents. Their relative low price, accessibility, reusability and low toxicity have contributed to a growing market trend for zeolites, which is expected to keep rising until 2020 [4].

Zeolites are crystalline aluminosilicate porous materials that have an infinite three-dimensional framework structure. The zeolite structure is composed of $TO_4$ tetrahedra that are connected by the sharing of oxygen atoms and where T represents a Si or Al atom [5] with Si/Al ≥ 1, in accordance with the Loewestein rule [6]. $SiO_4$ tetrahedra are neutrally charged unlike $AlO_4$ tetrahedra, which have a net negative charge of (-1). This net negative charge is countered by loosely-held extra-framework cations of H or of alkali or alkali-earth metals, such as Na, K, Mg or Ca [5]. The linking of the $TO_4$ tetrahedra originates channels and cavities of molecular dimensions in the zeolite structure that are occupied by the cations and water molecules, and constitute the zeolite's pores [5]. The zeolites' high thermal and hydrothermal stability allows them to be used as catalysts under severe temperature conditions. Their microporous structure of channels and cavities provides an expansive internal surface area, in which there is a high concentration of active sites, whose strength and number can be altered to suit the experimental conditions, and also shape selectivity, which allows preferential reaction pathways to be carried out by the effects of reactant/product size exclusion or transition state selectivity [7].

In addition to the properties mentioned above, the acidic nature of zeolites is what makes them the most widely used and characterised solid acid catalysts [8]. The acidity of zeolites is translated into the form of two types of acid sites: proton donor Brønsted acid sites (BAS) and electron pair acceptor Lewis acid sites (LAS). BAS can typically be found inside the zeolites' pores and consist of bridging hydroxyl (OH) groups, Si-O(H)-Al, as can be seen in Figure 2.

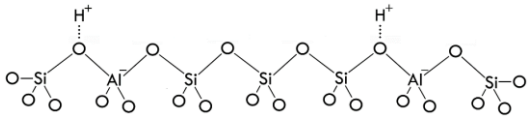


**Figure 2 –** Brønsted acid sites in zeolites

The activity of protonic groups is directly proportional to their strength, but also depends on their accessibility in terms of location and reagent molecule size, and proximity [9]. As the Si/Al ratio decreases the number of protonic groups increases, however the strength of each individual group decreases, on account of Al being less electronegative than Si, which results in stronger O-H bonds, i.e. weaker acidic groups [5] [9]. Other hydroxyl groups such as silanol (SiOH) groups that stem from framework defects or crystal termination, contribute, albeit in a lesser degree, to the overall acidity of the zeolite [9] [10].

LAS, although not as active as catalytic sites as protonic sites, can increase the acidic strength of their neighbouring BAS, by attracting electron density from BAS, lowering their O-H bond strength, which will increase their acidity [9] [11]. The majority of LAS in zeolites originate from EFAL, which are the outcome of dealumination caused by mild steaming or calcination, and Al structural defects, caused by dihydroxylation of BAS as a consequence of dehydration of the structure at high temperatures [8]. Other examples of LAS include extra-framework alkali cations [12].

Basicity in zeolites is an overall less industrially applied concept than acidity, and therefore a much less studied subject, however no less important, particularly in the scope of this work. In zeolites, most basic sites are associated with framework oxygen atoms due to their negative charge, that is a consequence of the presence of framework Al [12]. As such, the higher the framework Al content, i.e. the lower the Si/Al ratio is, the more basic centres the zeolite will have, and the more basic it will be, considering that Al has a lower electronegativity than Si [11]. Zeolite basicity also depends on the type of exchanged alkali cation: the less electronegative the extra-framework cation is, the more basic the zeolite will be [12] [13]. For alkali cation exchanged zeolites, basicity increases as follows [11] [12] [13]: Li < Na < K < Rb < Cs.

The zeolite used in this work was the protonic form of zeolite beta with a Si/Al ratio of 150 (BEA-150, $SiO_2/Al_2O_3$ = 300). Zeolite beta has a 12-membered ring system of mutually intersecting three-dimensional channels, a high thermal stability, Si/Al ratios that can go from 10 to more than 100, and it is usually in the form of small crystallites in the range of 20 – 50 nm [14] [15]. It is generally accepted that zeolite beta is a randomly ordered structure of two intergrown polymorphs, A and B [5] [16], with different stacking orders, as can be seen in Figure 3.

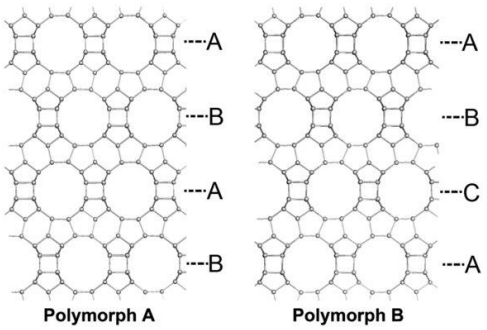


**Figure 3 –** Polymorphs A and B of zeolite beta [17]

Zeolite beta's disordered structure and small crystallite size render it a highly active catalyst [16] [15]. While a and b directions have unhindered channels, the channels in direction c are affected by the faulting caused by the stacking of the different polymorphs, and as a result exhibit an increased tortuosity [16]. The a and b directions' linear channels have pore openings of 7.5 × 5.7 Å, whereas the c direction's tortuous channels have pore openings of 6.5 × 5.6 Å [18]. Due to its unusual configuration and general small crystallite size, zeolite beta is a good catalyst, and as such has been used in a number of hydrocarbon-related processes [9] [14] [19]. Low Al, alkali ion-exchanged zeolites have been used in biodiesel production [20].

## 2. EXPERIMENTAL SECTION

Zeolite BEA-150 was acquired in its protonic form from *Zeolyst International* (reference CP811C-300). As it is in its protonic form and also due its low Al content, BEA-150 has an acidic nature.

### 2.1. MODIFICATION TECHNIQUES

To obtain a basic zeolite, K cations were introduced to substitute the native protons via two chemical treatments with aqueous solutions of $KNO_3$ or KOH, in varying K/Al ratios (1, 2 and 10): wet impregnation (WI) and ion exchange (IE). $KNO_3$ was obtained in powder form from *Alfa Aesar*, with an assay of 99% and KOH was obtained in pellet form from *Fisher Chemical*, with an assay of 86.15%.

WI was performed with a $V_{solution}/m_{zeolite}$ ratio of 1 mL/g. Each solution prepared was added to a zeolite sample in a glass beaker, and left stirring at 500 rpm for 15 minutes, followed by drying in an oven at 60 °C, for an average of 3 hours.

IE was carried out with a $V_{solution}/m_{zeolite}$ ratio of 20 mL/g, Each solution prepared was added to a zeolite sample in a glass beaker, and left stirring at 500 rpm for 24 hours to ensure a complete cation exchange. The samples were then centrifuged at 5000 rpm for 9 min, decanted, washed with deionized water and centrifuged again at 6000 rpm for 5 min, after which they were left to dry overnight in an oven at 60 °C. The samples prepared have been summarised in Table 1. All components were weighed in an *Ohaus Adventurer AR0640* analytical balance, with a maximum capacity of 65 g and a readability of 0.0001 g.

The eight samples were calcined in a *Carbolite Furnaces RHF 1600* furnace at 500 °C for 4 h, with a heating rate of 1 °C/min and a cooling rate of 5 °C/min until RT.

### 2.2. CHARACTERISATION TECHNIQUES

To study the physical and chemical properties of the zeolite samples, different techniques were used.

**SEM/EDS** were performed to evaluate the morphology and elemental composition of the samples. The instruments used to were a *Hitachi TM3000* microscope, with a *Bruker Quantax 70 EDS* analytical system attached for elemental analysis, operating at *Analy* or *15 kV* observation modes, respectively. All samples were pressed at approximately 0.5 ton before the analyses.

**XRD** patterns were collected to analyse the crystallinity of the samples. The equipment used was a *Bruker D8 Advance* with CuKα radiation ($\lambda$ = 1.5406 Å), 40 kV voltage and 40 mA amperage. The patterns were collected over a $2\theta$ range between 5 – 60°, with a coupled $2\theta/\theta$ scan type, a 0.02° step and a speed of 0.7 s/step.

**FTIR** was used to assess the acidity and basicity of the BEA-150 samples. Two probe molecules were used: Pyridine (Py, *ACROS Organics*, Assay = 99.5%) to study the acidity of the eight uncalcined samples and acetylene ($C_2H_2$, *BOC*, $Assay_{min}$ = 98.5%) to study the basicity of the eight calcined samples. All samples were pressed at approximately 0.5 ton into a self-supporting wafer ($\rho$ = 9 – 12 mg/cm$^2$) and loaded into an *in situ* IR cell. All experiments were run under vacuum. Py experiments were run following activation at 450 °C, for 300 min, with a heating rate of 1 °C/min from RT and a cooling rate of 5 °C/min until 150 °C (Py adsorption temperature); Py temperature programmed desorption (TPD) was run from 200 °C to a maximum of 450 °C in increments of 50 °C for 20 min, with a heating and cooling rates of 10 °C/min from and to 150 °C. $C_2H_2$ experiments were run following the same activation programme used for Py, letting the IR cell naturally cool to RT after the activation finished. $C_2H_2$ adsorption was done in two increments of approximately 0.5 and 5 torr, measured by way

**Table 1 –** Experimental BEA-150 samples prepared.

| Zeolite | Si/Al | Mod. Tech. | Exch. cation origin | K/Al | Sample name | Theoretical | | Experimental | |
|---|---|---|---|---|---|---|---|---|---|
| | | | | | | $m_{\text{BEA-150}}$ (g) | $m_{\text{K source}}$ (g) | $m_{\text{BEA-150}}$ (g) | $m_{\text{K source}}$ (g) |
| Beta, β (protonic form) | 150 | – | – | 0 | βOS | 2 | 0.0225 | 2.0032 | 0.0230 |
| | | WI | $KNO_3$ | 1 | βWIKNO$_3$1 | | 0.0288 | 2.0023 | 0.0299 |
| | | | KOH | 2 | βWIKOH2 | | 0.1438 | 2.0029 | 0.1440 |
| | | | | 10 | βWIKOH10 | | 0.0225 | 2.0033 | 0.0229 |
| | | IE | $KNO_3$ | 1 | βIEKNO$_3$1 | | 0.2255 | 2.0055 | 0.2279 |
| | | | | 10 | βIEKNO$_3$10 | | 0.0288 | 2.0028 | 0.0298 |
| | | | KOH | 2 | βIEKOH2 | | 0.1438 | 2.0030 | 0.1444 |
| | | | | 10 | βIEKOH10 | | 0.0225 | 2.0032 | 0.0230 |

of pressure gradient. $C_2H_2$ TPD was analysed at RT past 30 min of the last adsorption pressure, and when needed, at 100 °C for 20 min, at a heating and cooling rates of 10 °C/min from RT to 50 °C, respectively. The FTIR instrument used was a *Thermo Scientific Nicolet iS10* spectrometer, with a DTGS KBr detector, a KBr beamsplitter and an optical velocity of 0.4747 cm/s. All spectra were collected in transmission mode, with a resolution of 4 $cm^{-1}$ and 64 scans/spectrum. Background spectra were collected before each main spectra collection. Temperature programmes were set in a *Eurotherm 2416* PID Controller and the vacuum system used was a *Leybold PT50* turbomolecular pump system.

**$N_2$ sorption experiments** were run to evaluate the textural properties of the samples, such as surface area and pore size, volume and distribution. Each weighed sample ($m$ = 22 – 27 mg) was placed in a sample holder, a 9 mm large bulb cell (with an inner diameter of 7 mm), loaded into the instrument, outgassed and activated overnight at 350 °C for 300 min, with a heating rate of 1 °C/min from RT and a cooling rate of 5 °C/min until 100 °C, after which it was left to naturally cool down to RT and degassed. The instrument used was a *Quantachrome Autosorb C1*, with $N_2$ used as adsorptive gas. Data analysis was performed in the *Quantachrome ASiQwin 3.0*, and MultiPoint BET was used to calculate surface area, *t*-plot method to estimate micropore volume and micropore and external surface areas, and DFT to determine pore size distribution and diameter.

## 3. Results and Discussion

### 3.1. SEM/EDS

SEM images were collected in ordered to study the shape and size of the particles, whereas EDS measurements were taken to determine the elemental composition of the zeolite samples. The sets of images in Figures 4 and 5 illustrate the SEM images collected in varying magnifications (× 1k, 5k, 10k).

As can be seen from the images in 4 and 5, the particles are evenly distributed in the samples and are approximately homogenous in shape and size. From Figure 4A it can be concluded that the average particle size sits around 1 µm. As previously mentioned, the crystallite size for zeolite beta is usually in the rage of 20 – 50 nm [14] [15], which can suggest that the particles observed in Figures 4 and 5 are agglomerates of smaller crystallites. It can also be observed that chemical treatment does not appear to affect the particle size and shape, however, as picture clarity severely declines

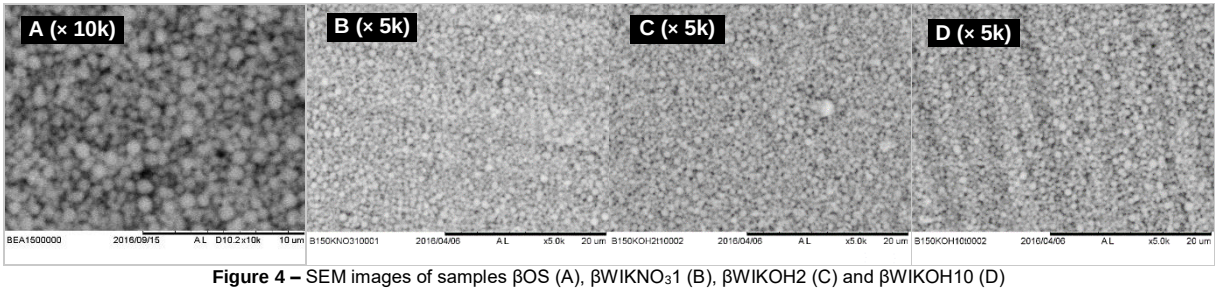


**Figure 4 –** SEM images of samples βOS (A), βWIKNO$_3$1 (B), βWIKOH2 (C) and βWIKOH10 (D)

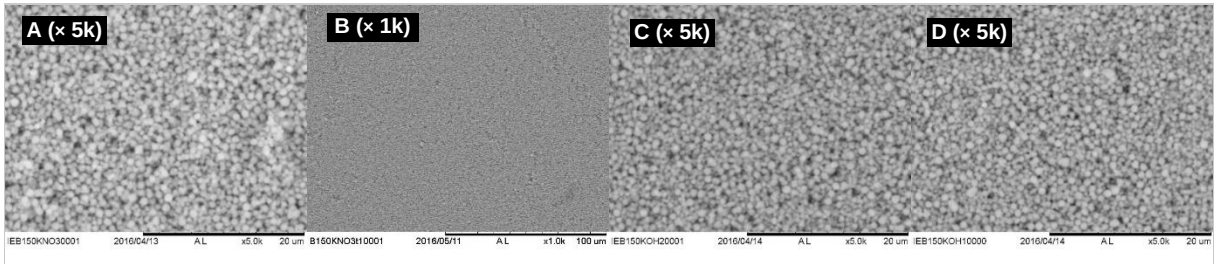


**Figure 5 –** SEM images of samples βIEKNO$_3$1 (A), βIEKNO$_3$10 (B), βIEKOH2 (C) and βIEKOH10 (D)

with magnification, this may not be accurate. Indeed, it is worth noting that from a magnification of 10k onwards the picture quality made it impossible to distinguish specific details of the particles' morphology.

Following SEM image collection, the samples were subject to EDS measurements, which provided elemental composition, with which it was possible to estimate Si/Al and K/Al ratios. Table 2 presents the Si/Al and K/Al ratios theoretically expected and experimentally obtained from EDS elemental analysis. It is worth noting that every experimental ratio shown in Table 2 represents the mean average of three distinct measurements taken in different areas of the corresponding sample, in order to achieve a higher degree of accuracy in the results.

**Table 2 –** Theoretical and experimental Si/Al and K/Al ratios of the original and modified samples

| Sample Name | Theoretical | | Experimental | |
|---|---|---|---|---|
| | Si/Al | K/Al | Si/Al | K/Al |
| βOS | 150 | – | 76.9 | – |
| βWIKNO$_3$1 | | 1 | 75.8 | 0.6 |
| βWIKOH2 | | 2 | 77.9 | 1.1 |
| βWIKOH10 | | 10 | 79.2 | 5.4 |
| βIEKNO$_3$1 | | ≤ 1 | 84.1 | 0.4 |
| βIEKNO$_3$10 | | ≤ 1 | 72.8 | 0.7 |
| βIEKOH2 | | ≤ 1 | 69.6 | 0.9 |
| βIEKOH10 | | ≤ 1 | 75.6 | 4.8 |

As can be seen in Table 2, despite being consistent with each other, the experimental results for the Si/Al and WI K/Al ratios of all samples are approximately half of what they should be. After further testing this has been attributed to the SEM/EDS apparatus used being incapable of accurately detecting an amount of Al as low as the one found in BEA-150. The IE K/Al ratios are all within the maximum expected value, with the exception of the last sample, βIEKOH10, that is circa five times higher than expected. This can be explained by the large molar excess of KOH, a strong base, added to this sample. The KOH, in addition to reacting with the bridging OH groups in the zeolite, thus exchanging $H^+$ with $K^+$, can also be reacting with SiOH groups, increasing the amount of $K^+$ cations in this sample, therefore resulting in a K/Al greater than the theoretical limit of 1. This hypothesis can be evaluated by the analysis of FTIR spectra in the following pages. It is worth noting that even though sample βIEKNO$_3$10 was also prepared with a molar excess of 10 in regards to Al, $KNO_3$ is an ionic salt that is practically neutral in aqueous solution, and therefore would not react with SiOH groups.

### 3.2. XRD

XRD patterns were taken to study the crystallinity of the sixteen uncalcined and calcined BEA-150 samples. This provided a better understanding of the effect calcination has on the different samples.

The XRD patterns of the eight uncalcined original and modified BEA-150 samples can be found in Figure 6. The well-defined characteristic peaks of zeolite beta can be seen in Figure 6 [21]. Furthermore, it can also be concluded that the BEA-150 zeolite samples used are composed of approximately 50 – 60% polymorph B [21].

Minor noise and background interferences were detected in all patterns, which suggests that the material is amorphous to some extent. The broad peaks observed are an indication of this structure's disordered nature, particularly peak number 1 in Figure 6, which corresponds to the reflection of the crystallographic plane (001). The patterns for the samples that have been treated with KOH show a clear loss of crystal structure that can be attributed to desilication caused by this strong base, which results in the destruction of the structure [22]. The five peaks numbered in Figure 6 have been attributed to the crystallographic planes listed in Table 3 [18].

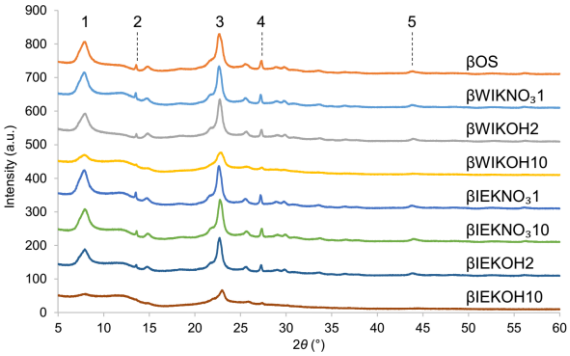


**Figure 6 –** XRD patterns of the eight uncalcined samples

**Table 3 –** Crystallographic planes identified on the beta samples [18]

| Peak | 2θ (°) | Crystallographic plane |
|---|---|---|
| 1 | 7.8 – 8.0 | (001) |
| 2 | 13.5 – 13.6 | (004) |
| 3 | 22.4 – 23.0 | (302) |
| 4 | 27.1 – 27.4 | (008) |
| 5 | 43.6 – 44.5 | (600) |

To better compare the effects of each modification treatment, a relative crystallinity was calculated according to Equation 1, using the original sample, βOS, as reference. The results are shown in Table 4.

$$\text{Rel. Cryst. (\%)} = \frac{\sum_{i=1}^{5}(\text{Intensity}_i)_x}{\sum_{i=1}^{5}(\text{Intensity}_i)_{\beta\text{OS}}} \times 100 \qquad (1)$$

**Table 4 –** Relative crystallinity of the modified BEA-150 samples in regards to βOS

| Sample | Relative Crystallinity (to βOS) |
|---|---|
| βWIKNO$_3$1 | 108% |
| βWIKOH2 | 94% |
| βWIKOH10 | 68% |
| βIEKNO$_3$1 | 113% |
| βIEKNO$_3$10 | 104% |
| βIEKOH2 | 91% |
| βIEKOH10 | 48% |

As can be seen in Table 4, the samples modified with $KNO_3$ demonstrate a slight increase in relative crystallinity, when compared to the original sample βOS (in its protonic form). This can be explained by the fact that K is a much heavier atom than H and heavier atoms are stronger X-ray scatterers [23], making the former's contributions to the diffraction intensities higher than the latter's. The exception to this, in the scope of this work, is the contributions of K to the XRD patterns when its source is KOH, seeing that, as mentioned before, KOH promotes desilication, and therefore loss of crystallinity by structure collapse. Indeed, the results determined by Equation 1 for the samples treated with KOH show a loss of crystallinity in comparison with the original sample, βOS, which was already noticeable in Figure 6.

To better compare the effect of calcination on the eight samples, Equation 1 was used to determine the relative crystallinity of each calcined sample in regards to its uncalcined form. The results are shown below in Table 5.

**Table 5 –** Relative crystallinity of the eight BEA-150 calcined samples in regards to their uncalcined forms.

| Sample | Relative Crystallinity (to uncalcined form) |
|---|---|
| βOS, calc. | 132% |
| βWIKNO$_3$1, calc. | 121% |
| βWIKOH2, calc. | 120% |
| βWIKOH10, calc. | 49% |
| βIEKNO$_3$1, calc. | 115% |
| βIEKNO$_3$10, calc. | 125% |
| βIEKOH2, calc. | 106% |
| βIEKOH10, calc. | 57% |

Overall, it can be seen that calcination improves the crystallinity of the samples, the exception being the samples treated with KOH with a K/Al molar ratio of 10. The increased crystallinity of calcined samples is related to improvements in contrast between the framework (high electron density) and the pores (zero electron density) [23] [24], which is caused by the elimination of extra-framework impurities in the pores during the calcination treatment. In the case of the samples treated with a 10-fold molar excess of KOH, as the structure is already severely damaged due to desilication, leaving Al atoms more exposed in the remaining structure, the calcination will cause dealumination [25], further disintegrating these samples' structures.

### 3.3. INFRARED

The IR data collected is presented below. All spectra were analysed in the 4000 – 1400 cm$^{-1}$ region. For the sake of consistency, all spectra were scaled to 10 mg/cm$^2$. Difference spectra were calculated by subtraction of the first samples' spectra (pre-adsorption), using a subtraction factor of 1.

#### ACIDITY

The IR spectra of the eight uncalcined original and modified samples, collected post-activation at 150 °C, can be found in Figure 7. These spectra were collected under vacuum after activation at 450 °C for 300 min.

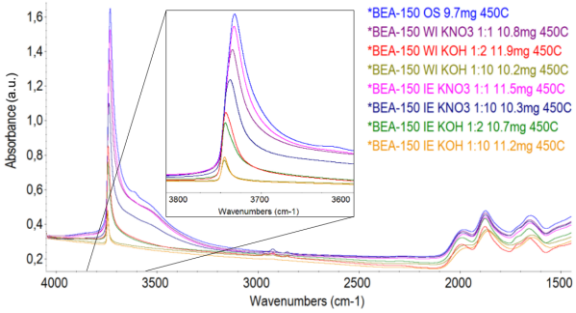


**Figure 7 –** IR spectra collected at 150 °C of the uncalcined activated BEA-150 samples, with an additional zoom in the SiOH region

Two major bands can be identified in Figure 7: the band characteristic of SiOH groups, located in the range of 3745 – 3732 cm$^{-1}$, and the band associated with bridging OH groups (BAS), seen only for βOS at 3611 cm$^{-1}$. The shoulder at around 3500 cm$^{-1}$ can be associated with the existence of perturbed SiOH groups, particularly H-bonded SiOH nests, or with contaminants such as $H_2O$ or N compounds (OH and NH stretching frequencies, respectively). The small peaks seen at approximately 3000 – 2800 cm$^{-1}$ correspond to CH stretching vibrations, which should be related to organic contaminants in the samples. The large peaks around 2000 – 1600 cm$^{-1}$ are associated with Si and O overtones.

Examining Figure 7, it can be clearly seen that the intensity of the SiOH band decreases drastically with increase of K content, and that this decrease is further heightened when KOH is the source. These results confirm that KOH (and to a lesser degree $KNO_3$) is reacting with SiOH groups, originating SiOK groups, as had been theorised previously. This is the reason behind the increased K/Al ratio of sample βIEKOH10 (as a reminder, it is circa 5 when it should be ≤ 1). Furthermore, as the number of SiOH groups decreases, the peak intensity is gradually shifting to higher frequencies, which is an indicative of stronger bonds, i.e., decreased acidity. The SiOH band for the untreated sample, BEA-150 OS, is located at 3732 cm$^{-1}$ which corresponds to internal SiOH groups due to structural defects [26], characteristic of the disordered structure of zeolite beta.

To study the acidity of the BEA-150 samples, Py was used as probe molecule. The difference spectra of the adsorption of this probe molecule can be seen below in Figure 8. The IR bands associated with Py adsorption on zeolites are commonly found in the frequency range of 1700 – 1400 cm$^{-1}$. Figure 9 displays a zoom in this IR region of the difference spectra in Figure 8. Twelve peaks have been identified in the spectra in Figure 9 and summarised in Table 6.

Difference spectra allow a better analysis of the existing peaks that could otherwise be difficult to accomplish. Indeed, and unlike in the spectra of Figure 7, in Figure 8 it is possible

to visualise the existence of a small BAS peak in spectrum E (sample βIEKNO$_3$1, “BEA-150 IE KNO3 1:1”) that has reacted with Py, resulting in a negative peak at 3611 cm$^{-1}$.

Examining Figure 9, it can be seen that the samples treated with KOH (spectra C, D, G and H) present no PyH$^+$ peaks (peaks 1 and 7), which shows that there are no BAS in those samples, and although a small amount of LAS can be found, basicity appears to have been achieved. The spectra of the samples treated with KNO$_3$ (B, E and F) show small PyH$^+$ peaks in comparison with the original sample’s spectrum (A), which was to be expected; furthermore, it can be concluded that given the absence of BAS in spectra B and F (in Figure 8), PyH$^+$ peaks correspond to weaker acidic interactions, such as those between Py and SiOH groups. In IE mobile species like EFAL tend to be removed in the excess solution, and therefore, PyL in the corresponding spectra may be related to other types of LAS, such as extra-framework cations or Al in structural defects.

Peak 4 appears only in spectra B, E and F, and it can be suggested that it is related to a weak type of PyL

Peak 5 is present in all spectra of the modified samples, with the exception of spectrum E, which is an indicative that this peak is related to an interaction of Py with K ions, that exist in inferior quantities in the sample of spectrum E. Furthermore, considering the spectra in Figure 7 it can be suggested that this interaction corresponds to a physisorption

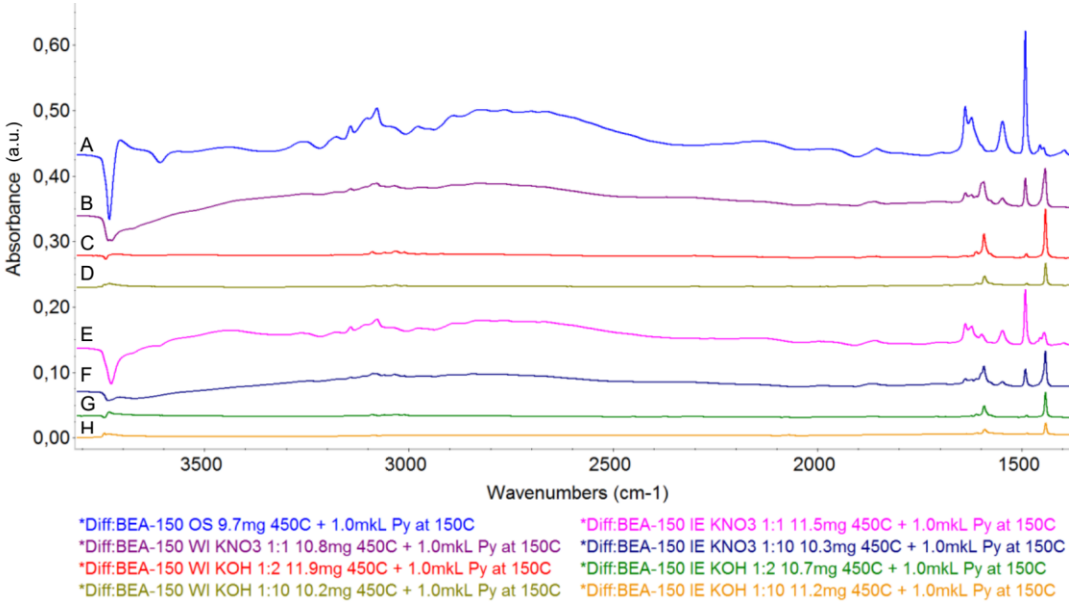


**Figure 8 –** Difference spectra of pyridine post-adsorption

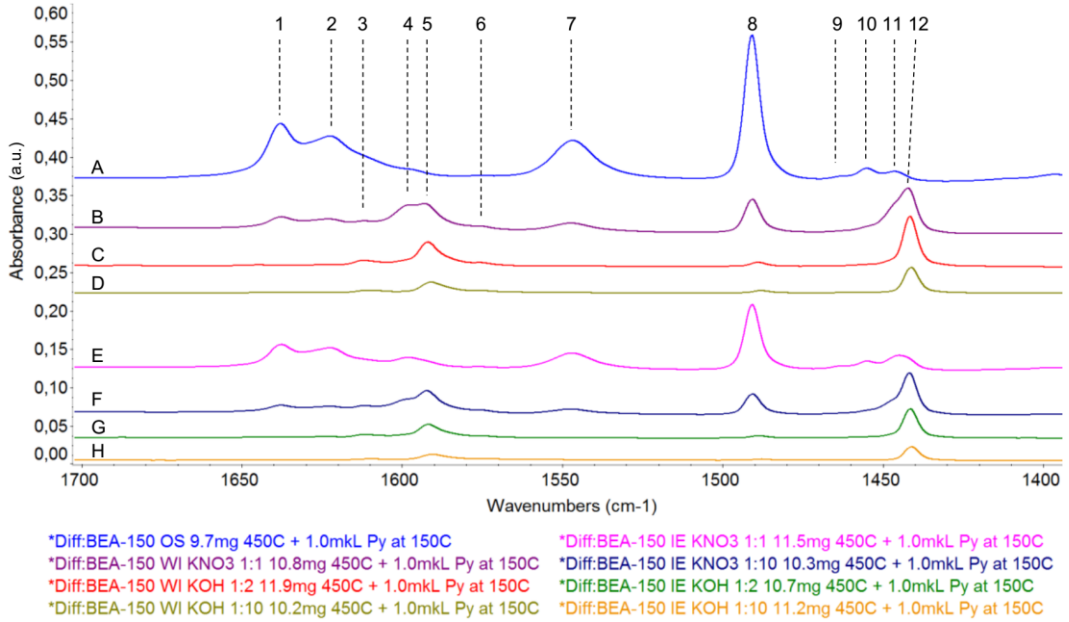


**Figure 9 –** Difference spectra of pyridine post-adsorption (zoom in the 1700–1400 cm$^{-1}$ region)

**Table 6 –** Pyridine adsorption peaks in the IR region of 1700 – 1400 $cm^{-1}$

| Peak | *v* ($cm^{-1}$) | Spectra | Species |
|---|---|---|---|
| 1 | 1638 | A B E F | $PyH^+$ (8a vibrational mode, $\nu_{CC}$) [27] |
| 2 | 1622 | A B E F | PyL (8a vibrational mode, $\nu_{CC}$) [28] [27] |
| 3 | 1612 | B C D E F G | PyL (8a vibrational mode, $\nu_{CC}$) [27] |
| 4 | 1599 | B E F | Suggestive of weak PyL (8a vibrational mode, $\nu_{CC}$) [27] |
| 5 | 1592 | B C D F G H | Suggestive of Py physisorbed to K (in SiOK groups) |
| 6 | 1575 | B C E F G | PyL (8b vib. mode, $\nu_{CC}$); H-bond to weak acid sites [27] |
| 7 | 1547 | A B E F | $PyH^+$ (19b vibrational mode, $\nu_{CN}$) [27] |
| 8 | 1491 – 1489 | A B C D E F G H | $PyH^+$, PyL and H-bond (19a vib. mode, $\nu_{CN}$) [28] [27] |
| 9 | 1463 | A E | Iminium ions [28] [29] |
| 10 | 1456 | A E | PyL (19b vibrational mode, $\nu_{CN}$) [28] [27] |
| 11 | 1446 | A B E F | Py physisorbed to H (can be considered PyL) [28] [30] |
| 12 | 1443 – 1441 | B C D F G H | Py physisorbed to K (can be considered PyL) [30] |

of Py in SiOK groups, and, as such, this could be the reason for the absence of peak 5 in spectrum E (Figure 7 shows an almost null decrease in SiOH groups in the spectrum of sample βIEKNO$_3$10, "BEA-150 IE KNO3 1:1").

Peak 6 appears in spectra B, C, E, F and G, which correspond to K-containing samples that do not show severe structural damage, and can be attributed to weak PyL or H-bond to remaining (and extremely weak) acid sites.

Peak 7 represents the most notable $PyH^+$ peak, which corresponds to C-N vibrations, and its appearance only in spectra A, B, E and F, reinforces that only these samples have a certain degree of acidity left.

Peak 8 appears in all spectra in different intensities; in spectra C, D, G and H, that correspond to samples modified with KOH, this peak is slightly shifted to lower frequencies which can be an indicative of these samples' basicity in comparison with the other samples. In these spectra peak 8 would correspond to extremely weak PyL or H-bond to weak acid sites.

Peak 9 is associated with iminium (IM) ions generated from $H^+$ attack to PyL and appears only in spectra A and E, which suggests that the formation of IM ions is related to BAS and LAS. Indeed, it has been observed in Py-TPD that peak 9 increases with increasing desorption temperature, whereas, particularly peaks 7 and 10 (the latter being the most notable PyL peak, associated with C-N vibrations and only visible in spectra A and E) decrease with increasing temperature. Py-TPD has shown an almost complete Py desorption from BAS and an incomplete desorption from LAS.

The relative intensities (to post Py adsorption at 150 °C) of peaks 7, 9 and 10 for sample βOS (spectrum A, "BEA-150 OS") have been plotted as a function of temperature in Figure 10. The relative intensities of $PyH^+$ and IM ions show symmetrical parabolic trends, with a slight variation in intensity until a desorption temperature of 300 °C is reached, and a sharp decrease or increase, respectively, thereafter. This symmetrical trend shows that Py desorption from BAS is a crucial factor in the formation of IM ions; the steady decrease of PyL associated with peak 10 may indicate that these are not the only type of PyL responsible for the formation IM ions. The steepness of the desorption curve of Py from BAS is an indicative that there are strong acid sites in the original sample, βOS, as per the definition of BAS. The mild and incomplete desorption of Py from LAS is suggestive of the very strong nature of these sites.

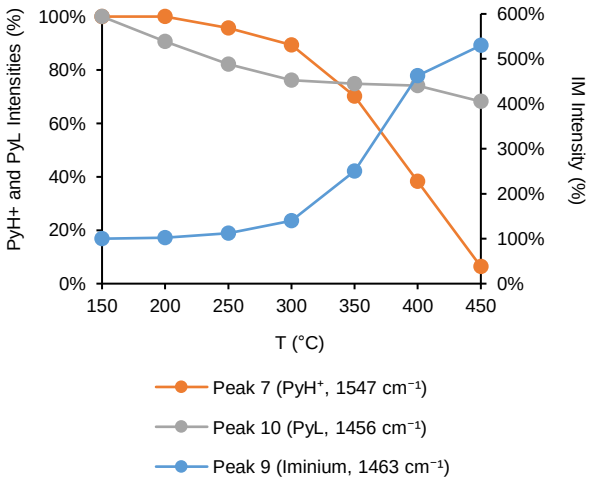


**Figure 10 –** Rel. int. of peaks 7, 9 and 10 in spectrum A (βOS)

Peak 11 appears in spectra A and E, and as a shoulder in spectra B and F and is associated with Py physisorbed to H and can be considered weak PyL.

Lastly, peak 12 corresponds to Py physisorbed to K (Py-K) and is visible in spectra B, C, D, F, G and H. Py-TPD has shown an almost immediate desorption of Py from K, which is an indicative of weak bonding.

### BASICITY

The IR spectra of the eight calcined (at 500 °C for 4 h) original and modified samples, collected post-activation at 30 °C, can be found in Figure 11. These spectra were collected under vacuum after activation at 450 °C for 300 min.

The spectra in Figure 11 follow the same trend in SiOH disappearance as the corresponding uncalcined samples' spectra in Figure 7, as was to be expected. However, the BAS band (3611 $cm^{-1}$) can now clearly be seen in the spectrum of sample βIEKNO$_3$1 ("BEA-150 IE KNO3 1:1") and it appears sharper for the spectrum of sample βOS ("BEA-150 OS"). This is a strong indication that there were indeed some contaminants associated with that frequency range that were obstructing the appearance of the BAS peak, that have now been removed by the calcination treatment. Furthermore, it can also be seen that the peaks at approximately 3000 – 2800 $cm^{-1}$, which are related to organic contaminants, have also decreased in comparison to those shown in Figure 7, having, likewise, been removed by calcination.

To study the basicity of the BEA-150 samples, acetylene ($C_2H_2$) was used as probe molecule. The difference spectra of this acidic probe molecule are shown in Figure 12. Three peaks have been identified in the spectra in Figure 12 and summarised in Table 7.

Peaks 1 and 2 are associated with the asymmetrical C-H bond stretching frequency (gas phase, $\nu = 3287$ $cm^{-1}$) [31]. Peak 1, visible in spectra B and C, corresponds to a π-complex formed between the C≡C bond and the K cations, and represents a blueshift of the gas phase frequency [31]. As peak 1 is associated with the existence of K in the samples, it is not clear why it does not appear in the other K-containing samples' spectra. It is worth noting, however, that it appears solely in the spectra of impregnated samples, with the exception of spectrum D in which the sample has been almost completely destroyed by the 10-fold molar excess of KOH. Although unlikely, it could be suggested that the complex in peak 1 is related to external surface interactions, as in WI some precursor cations may be left in the external surface of the zeolite, unlike in IE, where the exchanged cations tend to remain inside the pores. Peak 2, visible in all spectra, corresponds to an H-bond type connection with the framework basic oxygen, and represents a redshift of the gas phase frequency [31]. As basicity increases (i.e. K content in the sample) a slight redshift is noticeable in peak 2, which is due to bond weakening.

Peak 3 is associated with symmetrical C-C stretching frequencies ($\nu = 1974$ $cm^{-1}$) and should not, in theory, be seen in IR spectra. However, acetylene can adsorb unevenly onto the surface, causing a change in dipole moment, thus making symmetrical frequencies visible in the IR.

A small peak seen around 1700 $cm^{-1}$ is associated with a minor acetone contamination.

$C_2H_2$ desorption was run first at RT (≈ 25 °C) and then following a TPD at 100 °C. The latter was run to ensure a complete $C_2H_2$ desorption, although in most samples this was achieved after the first desorption at RT. The nearly instant desorption of $C_2H_2$ is an indicative of the expected weak bonding between the gaseous probe molecule and the solid support.

### 3.4. Sorption Experiments

$N_2$ sorption data is presented below. The MultiPoint BET plot was determined in the $p/p_0$ range of 0.02 – 0.1, which is lower than the common relative pressure range of linear applicability, 0.05 – 0.3 [32] [33] [34]. This is due to the samples being microporous, which shifts the linearity range to lower relative pressures [32] [34].

Figures 13 and 14 represent the $N_2$ sorption isotherms for the uncalcined and calcined samples, respectively. The isotherms obtained appear to be a combination of types I and IV: they present a high and steep incline for low relative pressures until circa 0.01, which is an indicative of the high amount of micropores in the structure of zeolite beta; from 0.01 until relative pressures of approximately 0.95 the multilayers are being adsorbed in larger pores (mesopores) until the zeolite's porous structure is entirely filled as $N_2$ capillary condensation occurs (final steep incline from $p/p_0$ of 0.95 to 1). The existence of hysteresis loops in all isotherms of the BEA-150 samples is an indicative of the existence of interparticle mesopores that could have been created by agglomeration of small crystallites [9]. The hysteresis loops observed, and therefore interparticle mesopores, increase for

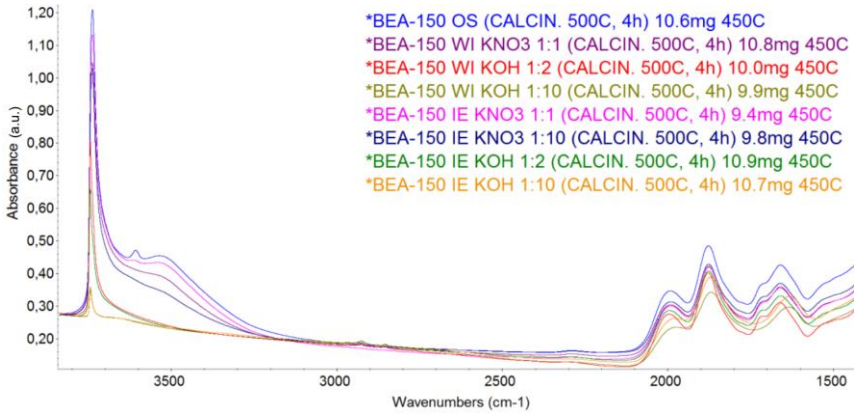


**Figure 11 –** IR spectra, collected at 30 °C, of the activated calcined original and modified BEA-150 samples

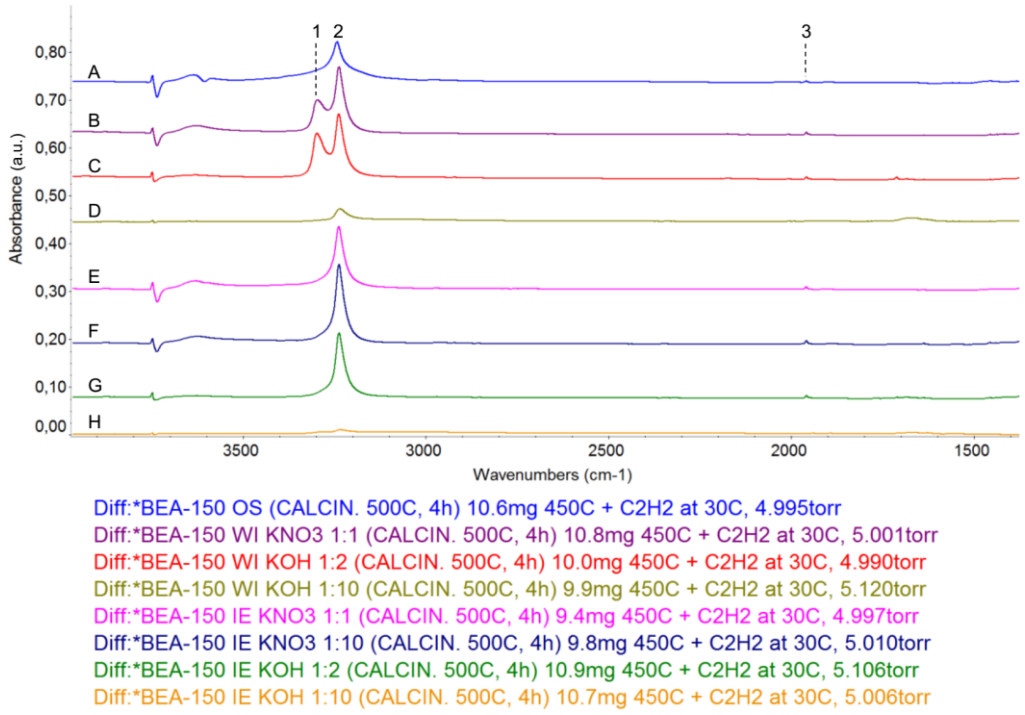


**Figure 12 –** Difference spectra of acetylene post-adsorption

**Table 7 –** Acetylene adsorption peaks

| Peak | *v* ($cm^{-1}$) | Spectra | Species |
|---|---|---|---|
| 1 | 3298 | B C | π-complex with $K^+$ (asymmetrical C-H stretching) [31] |
| 2 | 3243 – 3236 | A B C D E F G H | H-bond to framework O (asymmetrical C-H stretching) [31] |
| 3 | 1959 | A B C E F G | Symmetrical C-C bending |

samples treated with KOH and, for those, with increasing K content, which is evidence of the gradual destruction of the structure by this strong base, as had been already been seen. Once again, it is also clear that the samples treated with a 10-fold molar excess of KOH have been almost completely destroyed; they present a much lower micropore volume and bigger hysteresis loops than the other samples. In Figure 14 it can also be seen that calcined samples appear to adsorb higher amounts of $N_2$, which is a result of the thermal treatment that removes impurities and moisture from the samples, increasing the available space for $N_2$ adsorption.

Surface area was calculated using the MultiPoint BET and *t*-plot (external and micropore surface areas) methods. The results can be found in Figure 15 for the uncalcined samples and in Figure 16 for the calcined samples. The BET surface area for the original sample, βOS, is of the same order of magnitude as the value provided by the manufacturer (*Zeolyst International*, 620 $m^2/g$), and the difference may be attributed to variations in experimental setup and conditions. In general, BET surface area decreases with increasing K content, which would be expected considering that K, having a larger ionic radius than H, will occupy more space in the pores, hindering the progression and adsorption of $N_2$ molecules, thus resulting in lower BET surface areas. The exception to this trend is sample βIEKNO$_3$10, particularly the calcined form, which could be attributed to experimental error. It has also been suggested that the quadrupole moment of $N_2$ could be interacting with the K ions, resulting in its adsorption at different angles on the surface, thus increasing the overall adsorbed quantity [32]. This would not be the case with samples treated with KOH, which causes partial to severe structural damages and is conflicting with the suggestion that K hinders the progression and adsorption of $N_2$ into the pores. There may be a combination of these two suggestions happening with $N_2$ adsorption in K-containing samples.

For the uncalcined forms, it is possible to see that in the majority of samples the total surface area is approximately evenly split between external and micropore surface areas, as determined by the *t*-plot method, the exception being the samples treated with KOH with a K/Al molar ratio of 10, in which the micropore surface area consists of only a small percentage of the total surface area, as was to be expected, considering the collapse of micropores as a consequence of the destruction of these samples. After calcination, the micropore surface area appears to represent a bigger percentage of the total surface area, which was to be expected, due to the "cleansing" effect of calcination treatments, as mentioned earlier. For the calcined samples

treated with a 10-fold molar excess of KOH, there is no micropore surface area detected by the *t*-plot method, which is another indicative of structural collapse. Lastly, and as expected, the results in Figures 15 and 16 show an increase in total surface area for the calcined samples in comparison with the uncalcined forms (e.g.: 588 $m^2/g$ from 519 $m^2/g$ for βOS), with the exception of the destroyed samples (e.g.: 38 $m^2/g$ from 151 $m^2/g$ for βWIKOH10).

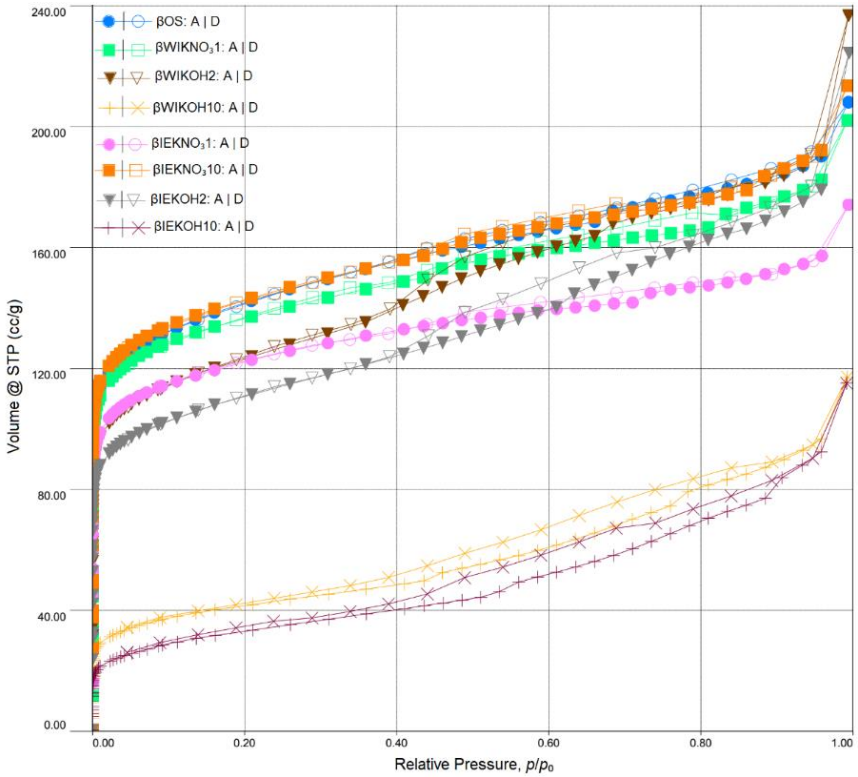


**Figure 13 –** $N_2$ sorption isotherms for the uncalcined BEA-150 samples

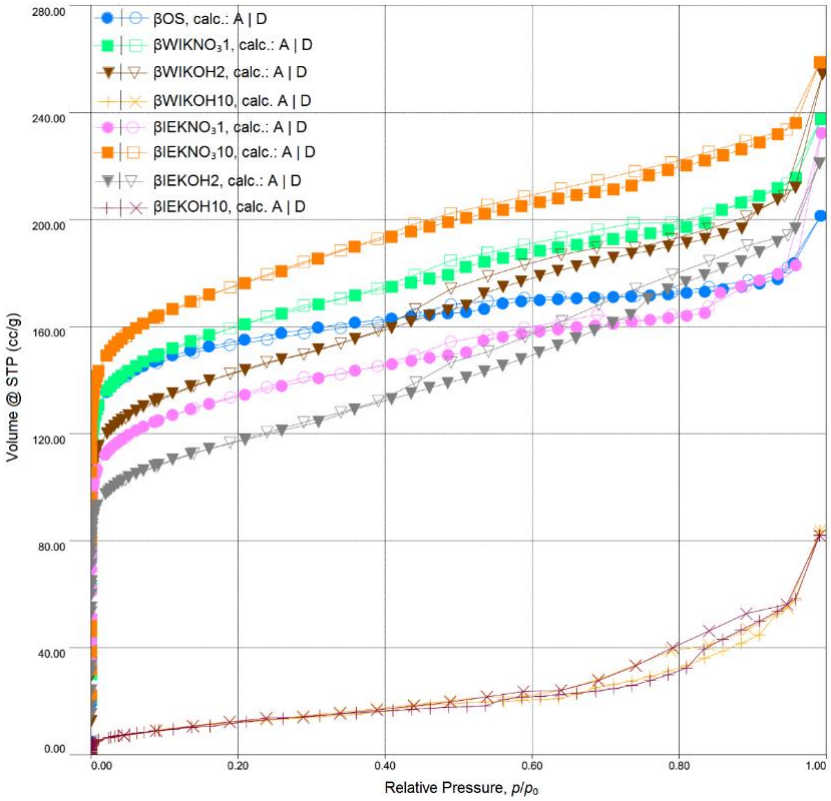


**Figure 14 –** $N_2$ sorption isotherms for the calcined BEA-150 samples

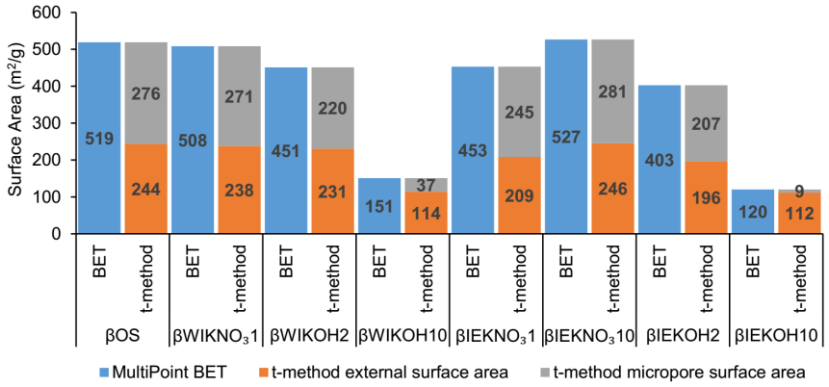


**Figure 15 –** MultiPoint BET and *t*-plot method (external and micropore) surface area for the uncalcined BEA-150 samples

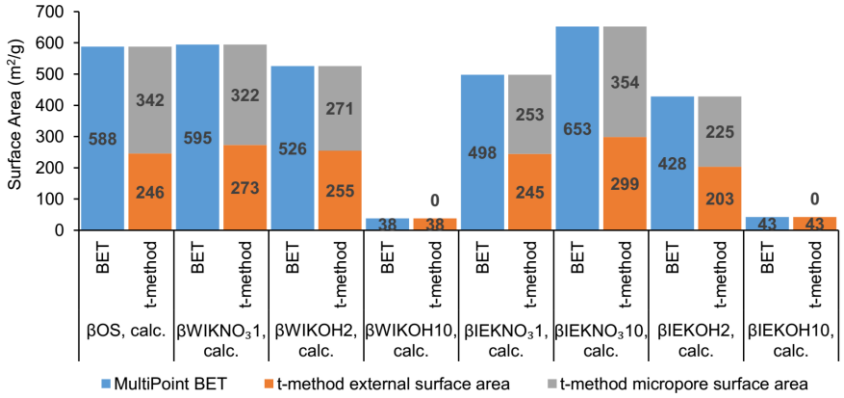


**Figure 16 –** MultiPoint BET and *t*-plot method (external and micropore) surface area for the calcined BEA-150 samples

Micropore volume has been calculated using the *t*-plot method and the results can be found in Figure 17. The same trend in values for the calcined samples with respect to the uncalcined forms, and of the influence of K source and content, both seen previously, can be seen in Figure 17. The micropore volume is smaller, although in the same order of magnitude, than previously published results [16] [35], which is an indication that the zeolite beta used in this work is more mesoporous than those referenced.

DFT was run (in the *Quantachrome ASiQwin 3.0* software) to determine pore size distribution and diameter. Figures 18 and 19 show the pore size distribution in the range of 0 – 28 Å for the uncalcined and calcined samples, respectively. Figure 20 presents the pore diameter determined for all samples.

Figure 18 shows that the majority of the uncalcined samples have micropores of approximately 8 Å with a smaller amount of micropores of approximately 10 Å, whereas the pore size distribution for the calcined samples in Figure 19 shows that the majority of pores have a size of approximately 10 Å, which is a consequence of the calcination treatment, as mentioned before. Overall, pore size is in accordance with previously published values [18]. Once again the destroyed samples fall off this trend. This is particularly notable for the calcined destroyed samples as can be seen in the chart in Figure 20, where the DTF calculation has determined a pore size of 67.9 Å for sample βWIKOH10 (calc.) and 101.3 Å for sample βIEKOH10 (calc.).

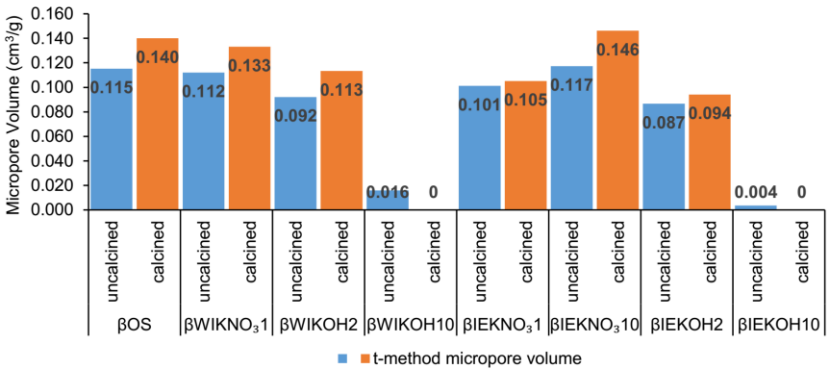


**Figure 17 –** *t*-plot method micropore volume for the uncalcined (■) and calcined (■) BEA-150 samples

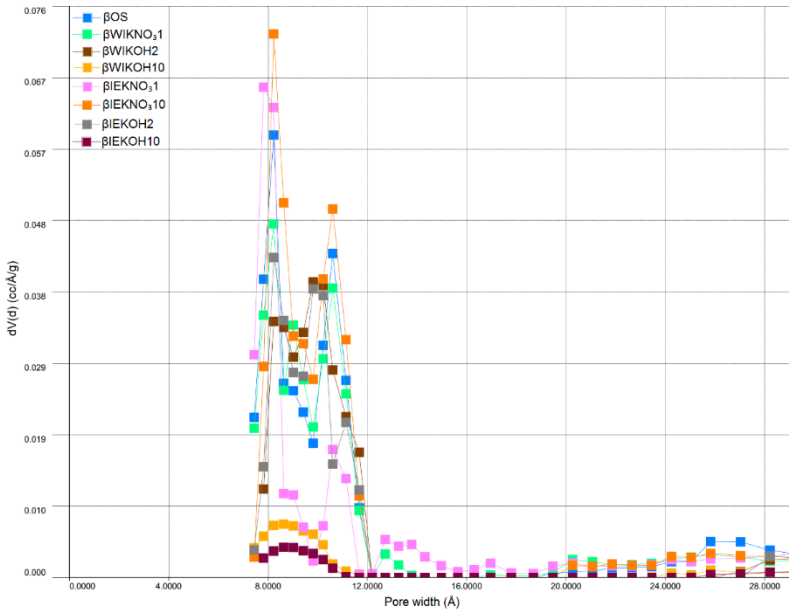


**Figure 18 –** DFT pore size distribution for the uncalcined BEA-150 samples

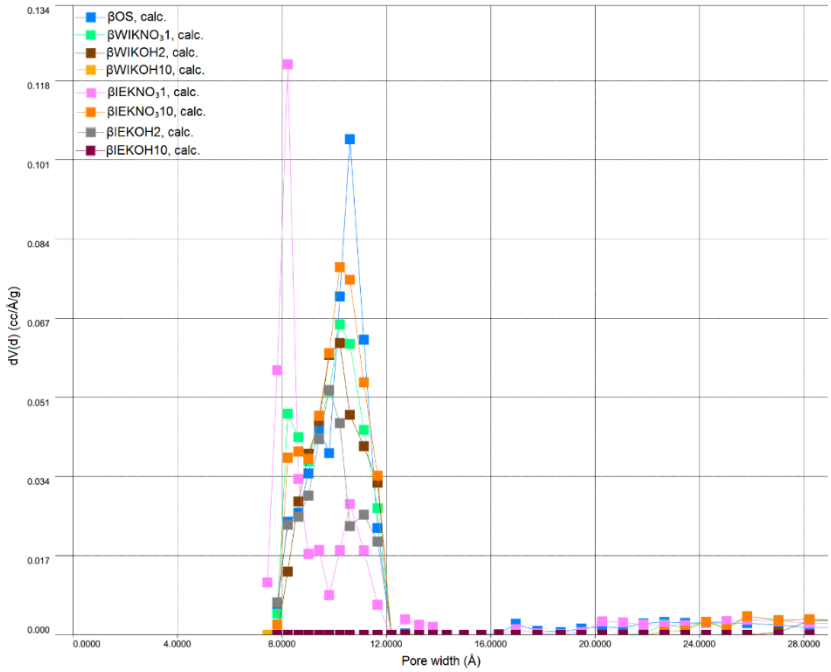


**Figure 19 –** DFT pore size distribution for the calcined BEA-150 samples

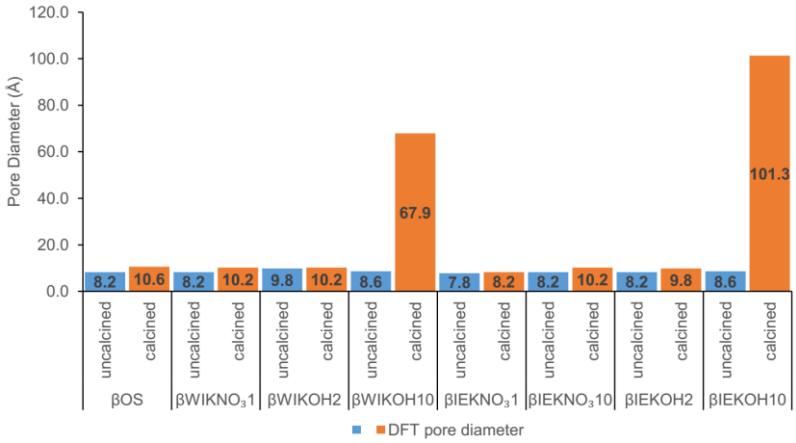


**Figure 20 –** DFT pore diameter for the uncalcined (■) and calcined (■) BEA-150 samples

## 4. CONCLUSION

The main objective of this work was to obtain a basic form of zeolite beta (BEA-150, Si/Al = 150) that could potentially be used as a basic heterogeneous catalyst for biodiesel production. This work was part of an ongoing project on the subject of biodiesel production, which also involves other researchers, and was developed in the Birchall Centre at Keele University. It consisted of the post-synthesis modification and characterisation of eight different samples of zeolite BEA-150.

The overall results have shown that basicity has been achieved, and that to a certain extent KOH is a more effective basicity inducing precursor than $KNO_3$. WI was found to be more effective for exchanged cation retention than IE.

It should be noted that careful consideration should always be taken in the choice of characterisation techniques, and their operating parameters. Often, spectroscopic techniques have certain limitations and results can be deceiving, until the employment of different techniques sheds further light on the overall results. The combination of different characterisation techniques allows for a much more complete and precise assessment of the properties of a single (or set of) sample(s).

Py and $C_2H_2$ have proven to be good probe molecules to assess the acidity and basicity of the samples. $N_2$ has also proven to be a good adsorptive gas, although ideally a monoatomic gas like Ar should be used to prevent unevenly surface adsorption.

Future work should now be conducted to further characterise the active sites, by determining their exact amount and location.

Nowadays more importance is being given to hierarchical zeolites, and that is mostly due to their exceptional versatile nature. The experimental results have shown that there are some mesopores in an otherwise microporous structure of the samples. These mesopores may have been created by desilication and dealumination phenomena or by agglomeration of smaller crystallites. Further research should be taken to implement the development of hierarchical BEA-150 zeolites.

## REFERENCES


[1] M. R. Avhad and J. M. Marchetti, “A review on recent advancement in catalytic materials for biodiesel production,” *Renewable and Sustainable Energy Reviews,* vol. 50, pp. 696-718, 2015.

[2] M. K. Lam, K. T. Lee and A. R. Mohamed, “Homogeneous, heterogeneous and enzymatic catalysis for transesterification of high free fatty acid oil (waste cooking oil) to biodiesel: A review,” *Biotechnology Advances,* vol. 28, pp. 500-518, 2010.

[3] D. W. Lee, Y. M. Park and K. Y. Lee, “Heterogeneous Base Catalysts for Transesterification in Biodiesel Synthesis,” *Catalysis Surveys from Asia,* vol. 13, pp. 63-77, 2009.

[4] Zion Research Analysis, December 2015. [Online]. Available: http://www.marketresearchstore.com/report/zeolite-market-z41101. [Accessed August 2016].

[5] H. van Bekkum, E. M. Flanigen, P. A. Jacobs and J. C. Jansen, Eds., Introduction to Zeolite Science and Practice, Second ed., Amsterdam, The Netherlands: Elsevier, 2001.

[6] W. Loewenstein, “The distribution of aluminium in the tetrahedra of silicates and aluminates,” *American Mineralogist,* vol. 39, pp. 92-96, 1954.

[7] A. Corma and A. Martínez, “The Chemistry of Catalytic Processes,” in *Zeolites for Cleaner Technologies*, M. Guisnet and J. Gilson, Eds., London, United Kingdom, Imperial College Press, 2002, pp. 29-55.

[8] E. G. Derouane, J. C. Védrine, R. Ramos Pinto, P. M. Borges, L. Costa, M. A. N. D. A. Lemos, F. Lemos and F. Ramôa Ribeiro, “The Acidity of Zeolites: Concepts, Measurements and Relation to Catalysis: A Review on Experimental and Theoretical Methods for the Study of Zeolite Acidity,” *Catalysis Reviews,* vol. 55:4, pp. 454-515, 2013.

[9] M. Guisnet and F. Râmoa Ribeiro, Zeólitos: Um Nanomundo ao Serviço da Catálise, Lisbon, Portugal: Fundação Calouste Gulbenkian, 2004.

[10] M. Boronat and A. Corma, “Factors Controlling the Acidity of Zeolites,” *Catalysis Letters,* vol. 145:1, pp. 162-172, 2015.

[11] J. Weitkamp and M. Hunger, “Acid and Base Catalysis on Zeolites,” in *Studies in Surface Science and Catalysis: Introduction to Zeolite Science and Practice (3rd Revised Edition)*, vol. 168, J. Čejka, H. van Bekkum, A. Corma and F. Schüth, Eds., Amsterdam, The Netherlands, Elsevier, 2007, pp. 787-835.

[12] S. Bordiga, C. Lamberti, F. Bonino, A. Travert and F. Thibault-Starzyk, “Probing zeolites by vibrational spectroscopies,” *Chemical Society Review,* vol. 44, pp. 7262-7341, 2015.

[13] Y. Ono and H. Hattori, Solid Base Catalysis, Berlin, Germany; Tokyo, Japan: Springer; Tokyo Institute of Technology Press, 2011.

[14] K. Shanjiao, G. Yanjun, D. Tao, Z. Ying and Z. Yanying, “Preparation and Characterization of Zeolite Beta with Low SiO2/Al203 Ratio,” *Petroleum Science,* vol. 4:1, pp. 70-74, 2007.

[15] J. P. Marques, I. Gener, P. Ayrault, J. C. Bordado, J. M. Lopes, F. Râmoa Ribeiro and M. Guisnet, “Infrared spectroscopic study of the acic properties of dealuminated BEA zeolites,” *Microporous and Mesoporous Materials,* vol. 60, pp. 251-262, 2003.

[16] J. M. Newsam, M. J. Treacy and W. T. Koetsier, “Structural Characterization of Zeolite Beta,” *Proceedings of the Royal Society of London A,* vol. 420, pp. 375-405, 1988.

[17] M. Tong, D. Zhang, W. Fan, J. Xu, L. Zhu, W. Guo, W. Yan, J. Yu, S. Qiu, J. Wang, F. Deng and R. Xu, “Synthesis of chiral polymorph A-enriched zeolite Beta with an extremely concentrated fluoride route,” *Nature: Scientific Reports,* vol. 5:11521, 2015.

[18] J. B. Higgins, R. B. LaPierre, J. L. Schlenker, A. Rohrman, J. Wood, G. Kerr and W. J. Rohrbaugh, “The framework topology of zeolite beta,” *Zeolites,* vol. 8:6, pp. 446-452, 1988.

[19] A. Simon-Masseron, J. P. Marques, J. M. Lopes, F. Ramôa Ribeiro, I. Gener and M. Guisnet, “Influence of the Si/Al ratio and crystal size on the acidity and activity of HBEA zeolites,” *Applied Catalysis A: General,* vol. 316, pp. 75-82, 2007.

[20] Y. Wang, D. Lee and B. Chen, “Low-Al Zeolite Beta as a Heterogeneous Catalyst in Biodiesel Production from Microwave-assisted Transesterification of Triglycerides,” *Energy Procedia,* vol. 6, pp. 918-921, 2014.

[21] International Zeolite Association, “Catalog of Disordered Zeoltie Structures: The Beta Family”.

[22] D. P. Serrano, J. M. Escola and P. Pizarro, “Synthesis strategies in the search for hierarchical zeolites,” *Chemical Society Reviews,* vol. 42, pp. 4004-4035, 2013.

[23] A. W. Burton, “Powder Diffraction in Zeolite Science: An Introductory Guide,” in *Zeolite Characterization and Catalysis: A Tutorial*, A. W. Chester and E. G. Derouane, Eds., New York, USA, Springer, 2009, pp. 1-64.

[24] R. E. Morris and P. S. Wheatley, “Diffraction Techniques Applied to Zeolites,” in *Studies in Surface Science and Catalysis: Introduction to Zeolite Science and Practice (3rd Revised Edition)*, vol. 168, J. Čejka, H. van Bekkum, A. Corma and F. Schüth, Eds., Amsterdam, The Netherlands, Elsevier, 2007, pp. 375-401.

[25] K. Li, J. Valla and J. Garcia-Martinez, “Realizing the Commercial Potential of Hierarchical Zeolites: New Opportunities in Catalytic Cracking,” *ChemCatChem,* vol. 6:1, pp. 46-66, 2014.

[26] J. Datka, K. Tarach and K. Góra-Marek, “Acidic Properties of Hierarchical Zeolites,” in *Mesoporous Zeolites: Preparation, Characterization and Applications*, J. García-Martínez and K. Li, Eds., Weinheim, Germany, Wiley-VCH, 2015, pp. 461-496.

[27] F. Thibault-Starzyk and F. Maugé, “Infrared Spectroscopy,” in *Characterization of Solid Materials and Heterogeneous Catalysts: From Structure to Surface Reactivity*, vol. 1, M. Che and J. C. Védrine, Eds., Weinheim, Germany, Wiley-VCH, 2012, pp. 3-48.

[28] J. P. Marques, I. Gener, P. Ayrault, J. C. Bordado, J. M. Lopes, F. Râmoa Ribeiro and M. Guisnet, “Infrared spectroscopic study of the acid properties of dealuminated BEA zeolites,” *Microporous and Mesoporous Materials,* vol. 60, pp. 251-262, 2003.

[29] M. Guisnet, P. Ayrault, C. Coutanceau, M. F. Alvarez and J. Datka, “Acid properties of dealuminated beta zeolites studied by IR spectroscopy,” *Journal of the Chemical Society, Faraday Transactions,* vol. 93:8, pp. 1661-1665, 1997.

[30] J. A. Lercher and A. Jentys, “Infrared and Raman Spectroscopy for Characterizing Zeolites,” in *Studies in Surface Science and Catalysis: Introduction to Zeolite Science and Practice (3rd Revised Edition)*, vol. 168, J. Čejka, H. van Bekkum, A. Corma and F. Schüth, Eds., Amsterdam, The Netherlands, Elsevier, 2007, pp. 435-476.

[31] E. B. Uvarova, L. M. Kustov and V. B. Kazansky, “Basicity of zeolites: IR-spectroscopic study using adsorbed molecular probes,” in *Studies in Surface Science and Catalysis: Catalysis by Microporous Materials, Proceedings of ZEOCAT '95*, vol. 94, H. K. Beyer, H. G. Karge, I. Kiricsi and J. B. Nagy, Eds., Amsterdam, The Netherlands, Elsevier, 1995, pp. 254-261.

[32] P. L. Llewellyn, E. Bloch and S. Bourrelly, “Surface Area/Porosity, Adsorption, Diffusion,” in *Characterization of Solid Materials and Heterogeneous Catalysts: From Structure to Surface Reactivity*, vol. 1, M. Che and J. C. Védrine, Eds., Weinheim, Germany, Wiley-VCH, 2012, pp. 853-879.

[33] K. S. W. Sing, D. H. Everett, R. A. W. Haul, L. Moscou, R. A. Pierotti, J. Rouquerol and T. Siemieniewska, “Reporting Physisorption Data for Gas/Solid Systems,” in *Handbook of Heterogeneous Catalysis (Second, Completely Revised and Enlarged Edition)*, vol. 1, G. Ertl, H. Knözinger, F. Schüth and J. Wetikamp, Eds., Weiheim, Germany, Wiley-VCH, 2008, pp. 1217-1230.

[34] International Organization for Standardization, “Determination of the specific surface area of solids by gas adsorption - BET method,” ISO 9277:2010, Geneva, Switzerland, 2010-09-01.

[35] M. A. Camblor, A. Corma and S. Valencia, “Characterization of nanocrystalline zeolite Beta,” *Microporous and Mesoporous Materials,* vol. 25, pp. 59-74, 1998.